Polymer 53 (2012) 4827–4833

Contents lists available at SciVerse ScienceDirect

Polymer

journal homepage: www.elsevier.com/locate/polymer

Surface relief terraces and self-assembled nanostructures in thin block copolymer films with solvent annealing

Zhen-Yuan Guo [a], Mei-Syun Lin [a], Yang-Ting Chang [a], Ya-Sen Sun [a,*], Yeo-Wan Chiang [b], Chung-Yi Chou [b], Wei-Yen Woon [c], Min-Chiang Chuang [c]

[a] Department of Chemical and Materials Engineering, National Central University, Taoyuan 32001, Taiwan
[b] Department of Materials and Optoelectronic Science, Center for Nanoscience and Nanotechnology, National Sun Yat-Sen University, Kaohsiung 804, Taiwan
[c] Department of Physics, National Central University, Taoyuan 32001, Taiwan

ARTICLE INFO

Article history:
Received 5 May 2012
Received in revised form
15 August 2012
Accepted 21 August 2012
Available online 30 August 2012

Keywords:
Block copolymers
Phase transitions
GISAXS

ABSTRACT

We have investigated the temporal evolution of relief terraces and microphase-separated nanodomains in poly(styrene-*block*-ethylene oxide) P(S-*b*-EO) on silicon substrates (SiO_x/Si) annealed under toluene/butanol vapors. For thin films, solvent annealing causes the formation of relief terraces. With solvent annealing for 12 h, hexagonal arrays of nanospheres of three sizes are dominant over the surface morphology of relief-terraced microstructures with epitaxial packing. The coexistence of nanospheres of three sizes is ascribed to a morphology triggered by the constraint of the film thickness. Upon exposure to toluene/butanol vapors for 16 and 20 h, these nanospheres become metastable and grow further into nanocylinders lying on the surface. During dewetting, the undulations of the local thickness and the nanodomain transitions are inseparable, consequently forming relief terraces comprising multiple layers of lying nanocylinders. The mechanisms and causes of nanodomain transitions of varied routes in solvent-annealed P(S-*b*-EO) films are analyzed and discussed.

© 2012 Elsevier Ltd. All rights reserved.

1. Introduction

The self-assembly behavior in thin films of block copolymers (BCP) has been widely studied because BCP thin films have morphologies more diverse than those of bulk samples [1–8]. Fabricating BCP thin films by spin coating combined with annealing under a solvent vapor becomes a simple, robust and effective way to produce nanodomains with long-range lateral order or ordered patterns with diverse morphologies [9–36]. The swelling of BCP thin films with a solvent to a particular extent to decrease the glass transition temperature T_g of polymers imparts a chain mobility during the solvent annealing; highly ordered arrays are thus achievable with solvent annealing at low temperatures [9–14]. For BCP that thermally degrades easily at high temperatures, solvent annealing offers an alternative route to promote highly ordered arrays of nanodomains. Another advantage of solvent annealing is that, whereas thermal annealing inevitably leads BCP thin films to have equilibrium nanodomains, solvent annealing causes the formation of metastable nanostructures that can be preserved on the vitrification of constituted blocks after rapid evaporation of the solvent [13].

In addition to annealing in a solvent vapor of a single type, a selective swelling of one block or blocks in a BCP through the use of binary immiscible solvent vapors typically increases the variety of surface morphology and phase transition behavior. The reason is that the solvent uptake can alter the constituted volume fraction, mediate the interactions between constituted segments in a block copolymer, influence the interactions at BCP/air or BCP/substrate interfaces, and alter the film thickness [13,15–17,27]. Because of the interplay between the preferential interactions at both BCP/air and BCP/substrate interfaces and the thickness commensurability, a dewetting of BCP thin films commonly occurs to form micro-scaled relief terraces on a substrate if the film thickness is incommensurate with the intrinsic spacing of ordered nanodomains [37–41]. As a result, varied surface morphologies of nanodomains can be kinetically triggered by the film undulation of the thickness (terrace formation) [13,37,38]. In particular, the micro-scaled development of the terrace formation and the related nanoscale phase transitions can interplay to cause nanostructures of several types, which differ in domain shape, size or inter-domain distance, to coexist within a destabilized thin film [1–6,37,38]. Little is understood, however, about the interplay between dewetting-induced terraces and the buried nanostructures within thin films that are exposed to vapors of binary solvents of varied selectivity. We investigated the structural evolution of polystyrene-*block*- polyethylene oxide P(S-

* Corresponding author. Tel.: +886 3422 7151x34205; fax: +886 3425 2296.
E-mail address: yssun@cc.ncu.edu.tw (Y.-S. Sun).

0032-3861/$ – see front matter © 2012 Elsevier Ltd. All rights reserved.
http://dx.doi.org/10.1016/j.polymer.2012.08.051

b-EO) thin films with solvent annealing in mixed vapors of toluene and butanol. Our objective was to acquire an improved understanding of the self-assembly behavior of thin films under solvent annealing in mixed vapors of binary immiscible solvents.

2. Experimental section

2.1. Materials

P(S-*b*-EO), for which $M_n = 25.3$ kg/mol, the volume fraction of PS and PEO blocks being $f_{PS} = 71\%$ and $f_{PEO} = 29\%$, and PDI = 1.05, was purchased from Polymer Source, Inc. and used as received. Silicon wafers with one oxide layer (SiO_x/Si) whose dimension was 1.5 cm × 1.5 cm were cleaned in a piranha solution (3:7 v/v 30% H_2O_2:H_2SO_4) for 40 min, rinsed with deionized water, and dried under flowing N_2. P(S-*b*-EO) powder was dissolved in toluene. After completely dissolved is toluene, P(S-*b*-EO) films of varied thickness were prepared via spin coating at 2000 rpm for 30 s from polymer solutions of 0.7–1.5 mass %. In an attempt to control the ordering and spatial orientation of nanodomains with solvent annealing, each film was then placed in a sealed jar (110 mL) with saturated toluene/butanol vapor (0.07mL/ 0.03mL in two vials each) for a varied duration (12, 16 and 20 h) of solvent annealing, at a maintained temperature 17 °C and humidity less than 10% in a chamber. Toluene [δ = 18.2 $(MPa)^{0.5}$] is a highly selective, nonpolar solvent for the PS block [δ = 18.6 $(MPa)^{0.5}$] whereas butanol [$\delta = 20.2\ (MPa)^{0.5}$]; is the most selective solvent for the PEO block [$\delta = 20.2\ (MPa)^{0.5}$] [42]. Toluene ($P^{sat} = 18.53$ mm Hg at 17 °C) is more volatile than butanol ($P^{sat} = 4.01$ mm Hg at 17 °C) [43]. Preswelling of polymer film in water vapor prior to solvent annealing prevents severe dewetting [13]. Therefore, the thin films were preswollen in water vapor for 1 h to prevent or retard severe dewetting of polymer film under solvent annealing. To avoid the effect of solvent removal rate on the morphology of solvent-annealed thin films [44–46], the samples were instantaneously removed from the jar when the time of solvent annealing was reached.

2.2. Characterization

To observe nanodomains and dewetted morphologies, we investigated the surface of thin films with an atomic-force microscope (AFM, SPA400 Seiko) in the tapping mode. We used aluminum-coated silicon cantilevers of length 125 μm, width 30 μm and thickness 4 μm. The force coefficient was approximately 42 N/m and the resonance frequency used was 160 kHz. For optical microscopy (OM, Olympus BX-BLA2) measurements we used the reflection mode. Since surface morphologies obtained by OM and AFM only provide a localized view of the structural information with limited statistics, therefore for AFM and OM measurements the samples were scanned and recorded in multiple positions in order to obtain more images. Measurements of grazing-incidence small-angle X-ray scattering (GISAXS) were performed with a Nano-Viewer (Rigaku) using CuK_α X-rays (30 kV and 40 mA) with wavelength $\lambda = 1.54$ Å at the Instrument Center of National Central University (NCU) or with synchrotron source ($\lambda = 1.55$ Å at 8 keV) at beamline BL23A of National Synchrotron Radiation Research Center (NSRRC). GISAXS patterns at NCU (NSRRC) were collected with PLATUS 100 K of 83.8 × 33.5 mm^2 (MAR CCD detector) at incidence angle 0.2°, which is an optimal angle between the critical angles of samples and substrates. Since the beam size of X-rays at NSRRC was 0.8 mm (horizontal) × 0.3 mm (vertical) [47], grazing at 0.2° approximately yielded a shinning area of 0.8 mm (width) × 86 mm (length). The length of the shinning region is much larger than the size of the samples, which gives statistical information of microphase-separated nanodomains over several millimeters. The scattering vector, q ($q = 4\pi/\lambda\sin\theta$, with scattering angle θ), in these patterns was calibrated with silver behenate. Before GISAXS, thin films were immersed in methanol for 20 min to induce surface reconstruction to increase the scattering intensity. For the observation under transmission electron microscopy (TEM), thin films were stripped and floated onto the water surface and then recovered by copper grids. Staining was achieved by exposing the films to vapor of a 4% aqueous RuO_4 solution for 120 min. Bright field TEM images were obtained by mass-thickness contrast on a JEOL JEM-2100 TEM at an accelerating voltage of 200 kV.

3. Results and discussion

After P(S-*b*-EO) films were prepared by spin coating, these films revealed slight contrast variations in local areas of OM images (not shown), indicating that the initially spun films were not perfectly flat. The slight variation of film thickness might be due to an effect of spin coating from a volatile solvent [48]. Before solvent annealing, the initial morphology of the thin films reveals a disordered dimple-like pattern (not shown). The disordered dimple-like pattern indicates the formation of spherical micelles. The micelles have a single size distribution and short-range order, which are a kinetically trapped morphology as a result of fast solvent evaporation during the spin coating process, in agreement with recent observations [13]. After solvent annealing for 12 h, regions of the P(S-*b*-EO) film display two colors – purplish and greenish (Fig. 1a). The colors in the image are due to the constructive interference of white light with the film, the free surface and the substrate interface. As the colors displayed in the OM image of a film depend both on the thickness of the film and on the refractive indices of the film, substrates and atmosphere, the colors provide only a crude indication of the variation of the thickness. AFM measurements were thus undertaken to characterize the thickness of a film annealed for 12 h with the mixed solvent vapors. According to the AFM characterization, the light greenish color of reflection corresponds to thin regions, and the purplish to thick regions (Fig. 1b). This result indicates that, after solvent annealing for 12 h, the film stature attained discrete values to form flat islands of constant thickness (purplish regions) that appear dispersed on top of a P(S-*b*-EO) layer (greenish regions). Large-scale AFM topographic imaging along the boundary between such two regions reveals that the difference of stature is about 16 nm (Fig. 1b). Imaging in the purplish and greenish regions reveals disparate surface topographies; in the purplish and thick regions two sizes – mean diameters (D) = 22.4 and 11.7 nm, average inter-domain spacing λ = 67.9 and 34.2 nm [49] – of PEO nanodomains are dominant, whereas the thin brownish regions have nanodomains of mostly a single medium size (d = 17.0 nm) with λ = 38.5 nm [49]. All these nanodomains reveal a dot-like morphology. We propose that the dot-like nanodomains are not associated with perpendicularly oriented nanocylinders, because the film instability resulting from its incommensurability does not occur if the thin films consist of perpendicularly oriented nanocylinders [13]. For this reason, we propose that these nanodomains are associated with nanospheres. For brevity, we use notation S_I, S_{II} and S_{III}, to denote nanospheres of varied size in a sequence from large to small. Regardless of the domain size, nanospheres of the three types pack with hexagonal order. The AFM image near a crack displays a featureless layer underneath the nanospheres (Fig. 1e). A careful analysis indicates that the thickness of the featureless layer is approximately 6 nm, whereas the thick regions have thickness 60 nm (Fig. S1, Supporting Information). This featureless layer is due to a layer of P(S-*b*-EO) chains anchored with the surface of SiO_x/Si [13,28]. According to the OM and AFM observations, we propose that, upon solvent annealing in toluene and butanol vapors of 12 h, the destabilized

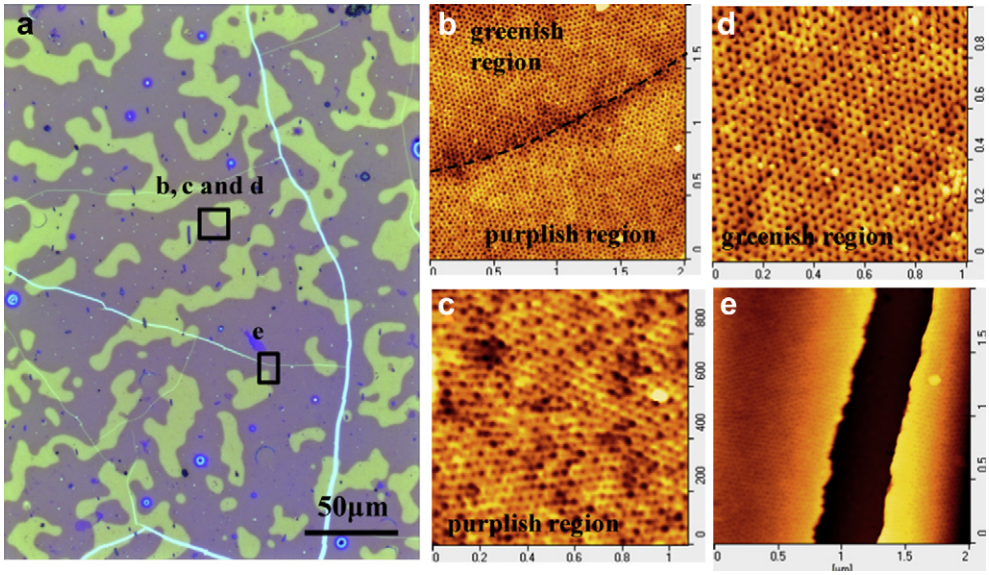

Fig. 1. Surface structure of a P(S-*b*-EO) thin film of initial thickness ≈54 nm after solvent annealing for 12 h in toluene and butanol vapors: (a) Reflection optical micrograph and (b–e) AFM topographies of the P(S-*b*-EO) film. Two squares shown in (a) respectively represent the areas for surface observations with an AFM.

film comprises a wetting layer anchored with SiO_x/Si on the bottom, a homogenous layer of S_{II} nanospheres in the middle and flat islands on the top. The morphology of the flat islands (purplish regions) is dominated by a lateral coexistence of S_I and S_{III} nanospheres.

We found also that the lateral coexistence of S_I and S_{III} nanospheres is present only when the film thickness is greater than the thickness of one layer of S_{II} nanospheres. For thin films of initial thickness comparable to the one layer thickness of S_{II} nanospheres, this small thickness suppresses the formation of S_I and S_{III} nanospheres and leads to a single morphology of S_{II} nanospheres (Fig. S2, supporting information). This result indicates that the S_I and S_{III} nanospheres might have a large barrier to develop near the substrate interface, whereas the S_{II} nanospheres preferentially grow at the substrate interface.

Furthermore, we suggest that the formation of those nanospheres with different sizes is attributed to thickness effect and gradient distribution of solvent concentration [12,18]. As mentioned, the initial morphology of as-spun thin films reveals a surface morphology of spherical micelles with a single size population. After solvent annealing for 12 h imposed on a P(S-*b*-EO) thin film of thick thickness, S_I might first appear on the top surface where the PEO nanospheres are bared on the air surface. By contrast, S_{III} forms below the S_I and possesses the PEO nanospheres embedded within PS matrix. Owing to the fast drying process after solvent annealing, the formation of nanospheres with different sizes was thus obtained due to the gradient distribution of the solvent contents along the substrate normal [12,18]. Similarly, because of slim film thickness, S_{II} exhibits that the PEO nanospheres embedded within the PS matrix.

Since Kim et al. discovered the coexistence of S_I and S_{III} PEO nanospheres within P(S-*b*-EO) films with solvent annealing in benzene and water vapors, little attention has been addressed to the packing of such nanospheres [13]. We found that nanospheres of three types coexisted within a destabilized film after solvent annealing for 12 h; S_I and S_{III} nanospheres coexisted laterally within flat islands and appeared in thick regions, whereas S_{II} nanospheres appeared as another structural layer preferentially near the substrate interface and existed in thin regions. It is still essential to know whether epitaxial packing or transitions between the three types exist, and to identify whether these nanodomains are equilibrium or metastable phases. A film solvent-annealed for 12 h was subsequently characterized with TEM and GISAXS. Fig. 2a,b shows plan-view TEM projection images for a thick purplish region, which display a regular network-like pattern of spherical nanodomains. This pattern is constructed of hexagonal arrays of spherical domains of two kinds with three sizes and inter-domain distances. The first kind is the hexagonal array of S_I nanospheres, in which each S_I nanosphere is preferentially separate from its nearest neighboring analogous species at largest distance ca. 61.5 nm. Within such a hexagonal array, each S_I PEO nanosphere is symmetrically surrounded by six S_{III} PEO satellite domains (marked with small and large white circles). The second hexagonal array comprised S_{II} spherical nanodomains of medium size (marked with red circles). It is well-established that when confined to a 2D thin film monolayer in a dry state, block copolymer spheres adopt an equilibrium closed-packed hexagonal arrangement [17,50,51]. By contrast, for the solvent-annealed P(S-*b*-EO) thin film, the hexagonal arrays and spherical nanodomains may not be at equilibrium under solvent annealing in vapors. The second kind has a small inter-domain spacing ca. 34.4 nm and possesses also an orientation rotated 30° with respect to the hexagonal array of S_I nanospheres. Those different layers with hexagonal lattice might have 30° rotational difference based on the packing energy consideration. With such an epitaxial orientation between the two hexagonal types, the $(10)_{II}$ spacing of the hexagonal array of S_{II} nanospheres is aligned with the $(11)_I$ spacing of the hexagonal array of S_I nanospheres. The small satellite PEO spheres (S_{III}) order with a quasi-hexagonal array, which has a specific orientational order rotated 15° with respect to the hexagonal array of S_{II} nanodomains.

Although AFM and TEM characterize the local spatial ordering of the nanodomains, a characterization of the spatial ordering on the nanoscale level over a macroscopic length scale is required. To characterize macroscopically the inner nanostructures of the solvent-annealed P(S-*b*-EO) films on SiO_x/Si, we measured GISAXS at angle 0.2°, which is an optimal angle between the critical angles of samples and substrates. Fig. 2c,d shows a 2D GISAXS pattern and 1D in-plane scattering profile, respectively. As Fig. 2c shows, a prominent feature is a modulation of the intensity along direction $q_\perp$ displayed by two streaks parallel to the $q_{//}$ direction. This

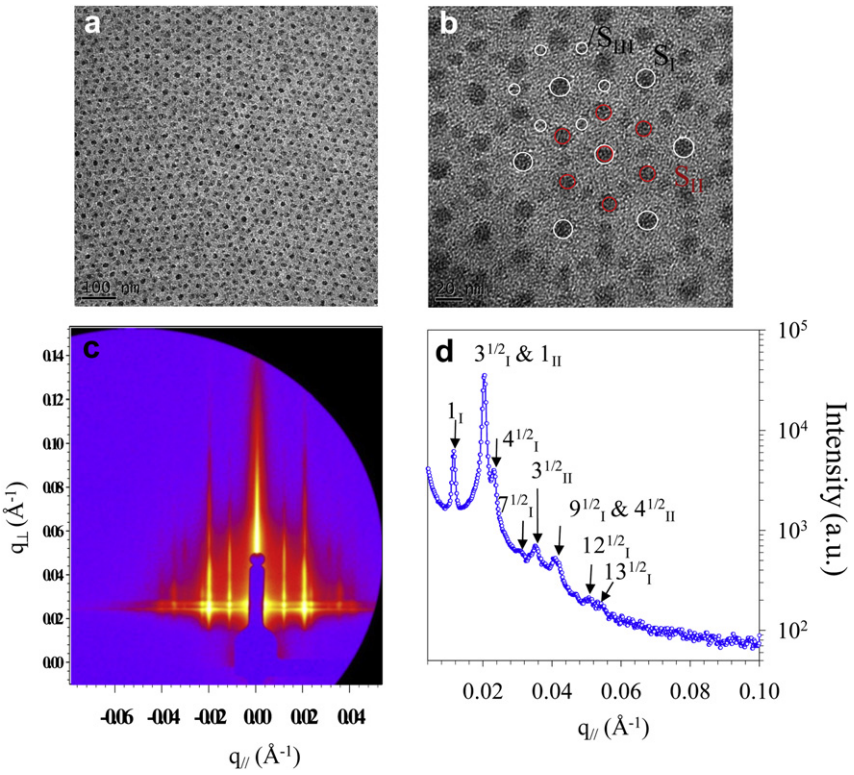

Fig. 2. (a, b) TEM plan-view images, (c) GISAXS pattern and (d) in-plane scattering profile of a P(S-*b*-EO) thin film of initial thickness ca. 54 nm after exposure to toluene and butanol vapor for 12 h. The TEM plan-view images correspond to the morphology of a purplish region, in which image-b has greater magnification of its TEM image. The dark regions correspond to PEO nanospheres stained with RuO_4.

discerned modulation is taken as an indication of a homogenous layer developed at the substrate interface [52–55]. Apart from the parallel streaks, the 2D GISAXS pattern for the film sample with exposure to toluene and butanol vapors for 12 h exhibits a series of Bragg diffraction-truncated rods typical of a strongly fiber-textured film, indicating that the nanodomains within the dewetted P(S-*b*-EO) film are highly oriented in the plane of the substrate (Fig. 2c). Typical characteristics of the Bragg diffraction-truncated rods of one-dimensional (1D) scattering intensity were clearly observed when a line scan cut along the horizon at $q_\perp = 0.0283$ Å^{-1} was imposed on the 2D GISAXS pattern to show a 1D profile. As Fig. 2d shows, the in-plane 1D GISAXS profile for the P(S-*b*-EO) film solvent-annealed for 12 h displays seven sharp diffraction peaks at $q_{//}$ ratio $1{:}3^{1/2}{:}4^{1/2}{:}7^{1/2}{:}\ 9^{1/2}{:}12^{1/2}{:}13^{1/2}$ with the first-order peak (labeled 1_I) being at $q_{//} = 0.0115$ Å^{-1}. The $q_{//}$ ratio indicates an in-plane two-dimensional (2D) hexagonal packing, and the peaks correspond to the (10), (11), (20), (21), (30), (22) and (31) planes of the hexagonal array. The inter-domain distance was determined to be 63.0 nm according to a formula $\lambda = 2\pi/q_{(10)} \times (4/3)^{1/2}$, in which $q_{(10)}$ corresponds to the position of the 1_I rod. This value 63 nm determined with GISAXS is consistent with the inter-domain distance for S_I nanodomains observed with a TEM. There is hence no argument against a proposal that the ratio of feature positions is associated with the hexagonal array of S_I nanodomains.

Two peaks at $q_{//} = 0.0203$ and 0.0408 Å^{-1} unusually appear intense intensities as compared to the two peaks indicated by 1_I and $7^{1/2}{}_I$ (Fig. 2d); In addition, there is still one peak at $q_{//} = 0.0349$ Å^{-1} that could not be designated as one feature for the hexagonal array of S_I and S_{III} nanospheres. We propose that these intense features are associated with a hexagonal array of S_{II} nanospheres. The reason is that a comparison of the positions of these three peaks indicates a ratio $1{:}3^{1/2}{:}4^{1/2}$ if the peak at $q_{//} = 0.0203$ Å^{-1} is taken as the other first-order feature. The intensity enhancement at those peaks is attributed to the possibility that the structure-factor scattering vectors of the hexagonal array of S_{II} nanospheres overlap with those of the hexagonal array of S_I nanospheres. According to the TEM images, we propose that the hexagonal array of S_{II} nanospheres possesses an orientation rotated 30° with respect to the hexagonal array of S_I nanospheres. Such an epitaxial orientation yields the GISAXS result in which the features (rods/peaks) corresponding to the $(10)_{II}$ and $(20)_{II}$ planes of the S_{II} hexagonal array overlap the features (rods/peaks) associated with the $(11)_I$ and $(30)_I$ planes of the S_I hexagonal array. This result explains further why the peaks at $q_{//} = 0.0203$ and 0.0408 Å^{-1} exhibit greater intensities than those labeled 1_I and $7^{1/2}_I$. We rationally propose that the set of intense features is associated with a hexagonal array of S_{II} nanospheres. According to the position of the second-order peak (at $q_{//} = 0.0203$ Å^{-1}), the inter-domain spacing of S_{II} nanospheres was determined to be 35.7 nm, in agreement with the inter-domain spacing of S_{II} nanodomains estimated from the TEM images.

Next we briefly explain why the $3^{1/2}$ reflection of S_I spheres and the primary peak of S_{II} spheres have the same q value. We speculate that the identical q value of the reflection of $(3)^{1/2}$ in S_I and the primary peak in S_{II} might be attributed to the epitaxial relationship of those hexagonal lattices with different sizes. Similar to the hexagonally perforated layer phase (HPL) with A-B-A or A-B-C packing [56,57], this epitaxial relationship should be dependent on the packing density and lattice spacing. Additional experiments to monitor nanodomain development with in situ GISAXS are in need to further elucidate the epitaxial packing mechanism during solvent annealing in vapors and solvent removal. Such experiments are in progress.

Fig. 3 is a schematic illustration to describe the in-plane hexagonal arrangements and epitaxial orientation of nanospheres of varied size and inter-sphere distance within a destabilized P(S-*b*-EO) film on SiO_x/Si. This illustration is proposed according to the

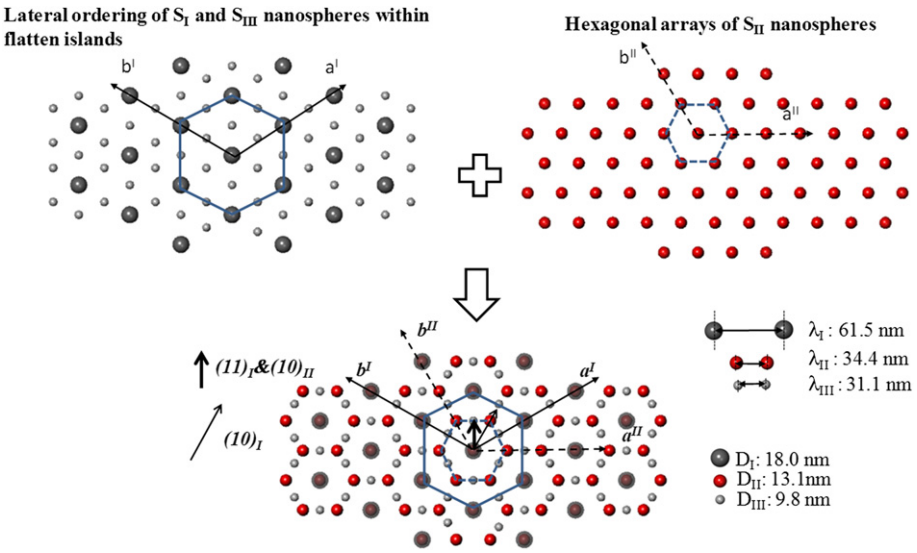

Fig. 3. Schematic illustrations of the spatial ordering for nanospheres of three types.

AFM, TEM and GISAXS characterizations. Dewetting-induced flat islands are composed of S_I nanospheres ordered as a hexagonal array and surrounded symmetrically by S_{III} nanospheres embedded within a PS matrix. Underneath the flat islands is a homogenous layer of S_{II} nanospheres with a hexagonal array. The two hexagonal arrays have an epitaxially oriented relation along the normal direction of the substrate, such that the S_I hexagonal array orients with a rotation 30° with respect to the S_{II} hexagonal array so that the $(10)_{II}$ planes of S_{II} nanospheres match with the $(11)_I$ planes of S_I nanospheres. We thereby observe a network-like, ordered morphology of nanospheres as viewed with the TEM along the normal direction of a film containing a layer of S_{II} nanospheres with hexagonal order epitaxially covered with flat islands comprised of S_I and S_{III} nanospheres.

Annealing for 16 and 20 h led to both the dissolution of the islands and the underlying layer to rearrange into a form of terraced microstructure (Fig. 4a,f and Fig. S3 for large-scale observations). Variations of the local stature of the film are accompanied by structural transitions. After 16 h of solvent annealing, we observed a splitting of the thickness of the homogenous film as-spun into developing terraces of varied height (Fig. 4a). In the following the terraces are denoted as T_0, T_1, T_2, T_3, T_4 and T_5 in order of increasing film thickness. The terraced surface structures and their statures were investigated with AFM. The lowest terrace T_0 exhibits a film thickness $d_{T0} \approx 7$ nm and a featureless morphology; this featureless surface is identified as a layer of P(S-*b*-EO) chains anchored with the hydrophilic surface of SiO_x/Si underneath the terraces T_1 to T_5. The thickness differences between the remaining terraces have a constant value, $\Delta d \approx 14 \pm 2$ nm. Terraces T_1 to T_5 exhibit mainly stripe-like nanodomains (Fig. 4c–e). The borders between adjacent terraces reveal that dot-like nanodomains and stripe-like nanodomains coexist. The stripe-like nanodomains are taken to indicate the formation of nanocylinders oriented parallel to the substrate surface. The transition from dot to stripe represents the transition from nanosphere to lying nanocylinder. The coexistence of spherical and cylindrical nanodomains demonstrates that the transition from sphere to cylinder takes place via nucleation and growth. For comparison, after solvent annealing a film for 20 h an instability causes a film to become terraced, composed mainly of multiple layers with nanodomains of a single type (i.e., lying nanocylinders) (Fig. 4h–j). The terrace of least thickness comprised the preferential wetting layer, thickness ~7 nm, anchored with the substrate (Fig. 4g).

The corresponding GISAXS pattern for the film annealed with a solvent for 16 h demonstrates that the scattering truncation rods are located at $q_{//} = 0.0197$ and 0.0394 Å^{-1}, which corresponds to $q_{//}$ ratio = $1:4^{1/2}$. The $q_{//}$ ratio is produced from the in-plane correlation of the nanocylinders within multiple layer terraces, as the thickness of the film is less than three layers of lying nanocylinders. From the position ($q_{//} = 0.0197$ Å^{-1}) of the principal rod, the inter-domain distance was estimated to be 31.9 nm; this value is comparable with the spacing of the $(10)_{II}$ planes. For the reason, we propose that the parallel-oriented nanocylinders developed via merging or fusion of nanospheres along $(10)_{II}$ planes, giving rise to the inter-cylinder spacing [14]. After further exposure to mixed vapors of toluene/butanol for 20 h, the films grew into multiple layers of parallel-oriented nanocylinders with inter-domain distance 30.2 nm. S_I and S_{III} nanospheres also transformed into lying PEO nanocylinders, but the spacing of the lying nanocylinders is comparable only with that of the nanocylinders developed from a transformation of S_{II} nanospheres. This result indicates that a transition to grow lying nanocylinders for S_I and S_{III} nanospheres did not proceed directly through the merging and fusion of nanospheres along the $(10)_I$ plane of S_I nanospheres; otherwise we should have observed lying nanocylinders with the large spacing corresponding to the spacing period of the $(10)_I$ plane of S_I nanospheres. Here we propose another mechanism of nanodomain transformation to explain the formation from S_I and S_{III} nanospheres to lying nanocylinders. Kim B et al. found that nanodomains of varied size can be obtained through varied routes of kinetic domain formations – large nanospheres via the coalescence of two PEO domains triggered by a thickness constraint, or small nanospheres through a chain rearrangement via the rapid diffusion of polymer chains [13]. In our experiments, we speculate that the S_I and S_{III} nanospheres transform into parallel-oriented nanocylinders proceeding through an intermediate stage of nanospheres of average size between the sizes of S_I and S_{III} nanospheres. The intermediate stage might originate from a chain rearrangement via diffusion of polymer chains, rather than from an inter-domain coalescence triggered by the confinement of the film thickness. At this intermediate stage, an exchange of BCP chains between S_I and S_{III} nanospheres leads to growing domains of another size and an inter-domain distance of spherical nanodomains. These spherical nanodomains are expected to be analogous to the S_{II} nanospheres in size and inter-domain distance, and also metastable. Prolonged

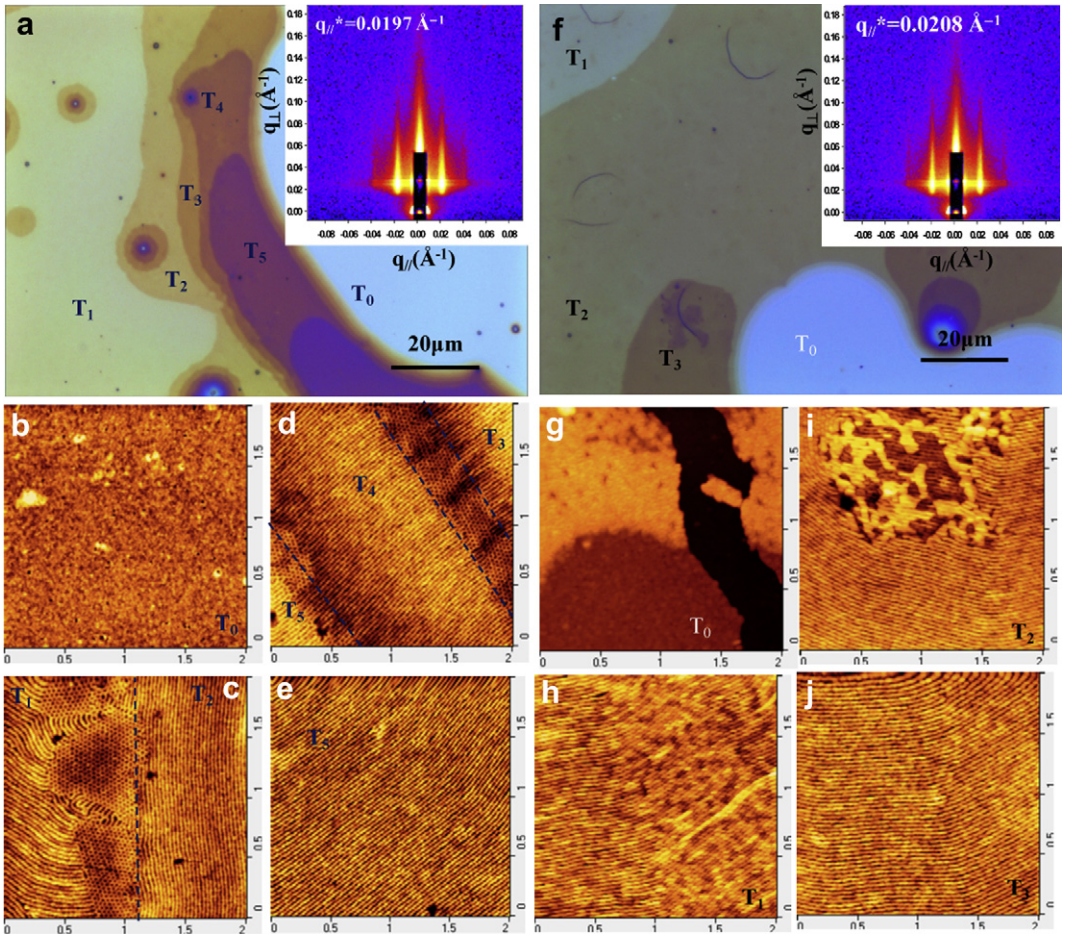

Fig. 4. Reflection optical micrograph (a, f) and AFM topographies (b–e and g–j) of P(*S*-*b*-EO) films of initial thickness ca. 54 nm annealed for 16 (a–e) and 20 h (f–j) in toluene and butanol vapors, respectively. The insets in OM images a & f correspond to 2D GISAXS patterns.

solvent annealing leads to lying nanocylinders that grow at the expense of nanospheres via a mechanism involving nucleation and growth. As a result, parallel-oriented nanocylinders with a short spacing were obtained even for the morphological transformation of S_I and S_{III} nanospheres.

4. Conclusions

In summary, we have investigated the temporal evolution of nanodomains within P(S-*b*-EO) films after solvent annealing in toluene/butanol vapors. At 12 h, solvent annealing causes dewetting to form flat islands of constant thickness covering a homogenous layer; this layer comprises an anchored layer of P(S-*b*-EO) chains at the interface of SiO_x/Si and one layer of S_{II} nanospheres with hexagonal order. In contrast, the flat islands exhibit a lateral existence of S_I and S_{III} nanospheres, in which the S_I nanospheres order with a hexagonal lattice. The nanospheres differ in domain size and inter-domain distance, but they pack together within the destabilized P(S-*b*-EO) film with a longitudinally epitaxial orientation. After solvent annealing for 16 and 20 h, the nanopheres grow further into lying nanocylinders via merging or fusion of S_{II} nanospheres along the $(10)_{II}$ planes through nucleation and growth. For S_I and S_{III} nanospheres, the transformation to form lying nanocylinders involves an intermediate stage developed by rearrangement of the domain size of nanodomains through the diffusion of polymer chains and then nucleation and growth.

Acknowledgments

National Science Council provided supports (NSC–100–2628–E–008–007-MY3 and NSC–100–2120–M–008-001-). We thank Dr. U-Ser Jeng, Dr. Chiu-Hun Su and Dr. Chun-Jen Su for their assistance in the GISAXS experiments at beamline BL23A at the NSRRC.

Appendix A. Supplementary data

Supplementary data related to this article can be found at http://dx.doi.org/10.1016/j.polymer.2012.08.051.

References

[1] Knoll A, Horvat A, Lyakhova KS, Krausch G, Sevink GJA, Zvelindovsky AV, et al. Phys Rev Lett 2002;89. 035501/1-4.
[2] Ludwigs S, Krausch G, Magerle R. Macromolecules 2005;38:1859–67.
[3] Lyakhova KS, Sevink GJA, Zvelindovsky AV, Horvat A, Magerle R. J Chem Phys 2004;120:1127–37.
[4] Horvat A, Lyakhova KS, Sevink GJA, Zvelindovsky AV, Magerle R. J Chem Phys 2004;120:1117–26.
[5] Huinink HP, Brokken-Zijp JCM, van Dijk MA, Sevink GJA. J Chem Phys 2000; 112:2452–62.
[6] Tsarkova L, Knoll A, Krausch G, Magerle R. Macromolecules 2006;39:3608–15.
[7] Knoll A, Lyakhova KS, Horvat A, Krausch G, Sevink GJA, Zvelindovsky AV, et al. Nat Mater 2004;3:886–91.
[8] Ludwigs S, Böker A, Voronov A, Rehse N, Magerle R, Krausch G. Nat Mater 2003;2:744–7.
[9] Park S, Lee DH, Xu J, Kim B, Hong SW, Jeong U, et al. Science 2009;323:1030–3.

[10] Park S, Kim B, Xu J, Hofmann T, Ocko BM, Russell TP. Macromolecules 2009; 42:1278–84.
[11] Cavicchi KA, Berthiaume KJ, Russell TP. Polymer 2005;46:11635–9.
[12] Kim SH, Misner MJ, Xu T, Kimura M, Russell TP. Adv Mater 2004;16:226–31.
[13] Kim B, Hong SW, Park S, Xu J, Hong SK, Russell TP. Soft Matter 2011;7:443–7.
[14] Hong SW, Gu X, Huh J, Xiao S, Russell TP. ACS Nano 2011;5:2855–60.
[15] Bang J, Kim SH, Drockenmuller E, Misner MJ, Russell TP, Hawker CJ. J Am Chem Soc 2006;128:7622–9.
[16] Bang J, Kim BJ, Stein GE, Russell TP, Li X, Wang J, et al. Macromolecules 2007; 40:7019–25.
[17] Tang C, Bang J, Stein GE, Fredrickson GH, Hawker CJ, Kramer EJ, et al. Macromolecules 2008;41:4328–39.
[18] Ho RM, Tseng WH, Fan HW, Chiang YW, Lin CC, Ko BT, et al. Polymer 2005;46: 9362–77.
[19] Paik MY, Bosworth JK, Smilges DM, Schwartz EL, Andre X, Ober CK. Macromolecules 2010;43:4253–60.
[20] Bosworth JK, Paik MY, Ruiz R, Schwartz EL, Huang JQ, Ko AW, et al. ACS Nano 2008;2:1396–402.
[21] Jung YS, Ross CA. Adv Mater 2009;21:2540–5.
[22] Jeong JW, Park WI, Kim MJ, Ross CA, Jung YS. Nano Lett 2011;11:4095–101.
[23] Jung YS, Chang JB, Verploegen E, Berggren KK, Ross CA. Nano Lett 2010;10:1000–5.
[24] Son JG, Chang JB, Berggren KK, Ross CA. Nano Lett 2011;11:5079–84.
[25] Chang CY, Wu PJ, Sun YS. Soft Matter 2011;7:9140–7.
[26] Chang CY, Lee YC, Wu PJ, Liou JY, Sun YS, Ko BT. Langmuir 2011;27:14545–53.
[27] Kim TH, Hwang J, Hwang WS, Huh J, Kim HC, Kim SH, et al. Adv Mater 2008; 20:522–7.
[28] Kim TH, Huh J, Park C. Macromolecules 2010;43:5352–7.
[29] Xuan Y, Peng J, Cui L, Wang H, Li B, Han Y. Macromolecules 2004;37:7301–7.
[30] Peng J, Wei Y, Wang H, Li B, Han Y. Macromol Rapid Commun 2005;26:738–43.
[31] Peng J, Xuan Y, Wang H, Yang Y, Li B, Han Y. J Chem Phys 2004;120:11163–70.
[32] Luo C, Huang W, Han Y. Macromol Rapid Commun 2009;30:515–20.
[33] Luo C, Huang W, Han Y. Macromol Rapid Commun 2009;30:1917–21.
[34] Kim S, Briber RM, Karim A, Jones RL, Kim HC. Macromolecules 2007;40:4102–5.
[35] Albert JNL, Bogart TD, Lewis RL, Beers KL, Fasolka MJ, Hutchison JB, et al. Nano Lett 2011;11:1351–7.
[36] Mokarian-Tabari P, Collins TW, Holmes JD, Morris MA. ACS Nano 2011;5: 4617–23.
[37] Lykhova KS, Horvat A, Zvelindovsky AV, Sevink GJA. Langmuir 2006;22:5848–55.
[38] Horvat A, Knoll A, Krausch G, Tsarkova L. Macromolecules 2007;40:6930–9.
[39] Grim PCM, Nyrkova IA, Semenov AN, ten Brinke G, Hadziioannou G. Macromolecules 1995;28:7501–13.
[40] ven Zoelen W, Polushkin E, ten Brinke G. Macromolecules 2008;41:8807–14.
[41] ven Zoelen W, Asumaa T, Ruokolainen J, Ikkala O, ten Brinke G. Macromolecules 2008;41:3199–208.
[42] Barton AFM. Chem Rev 1975;75:731–53.
[43] Munday EB, Mullins JC, Edie DD. J Chem Eng Data 1980;25:191–4.
[44] Hung H, Hu Z, Chen Y, Zhang F, Gong Y, He T, et al. Macromolecules 2004;37: 6523–30.
[45] Kim G, Libera M. Macromolecules 1998;31:2569–77.
[46] Albert JNL, Young WS, Lewis RL, Bogart TD, Smith JR, Epps TH. ACS Nano 2012; 6:459–66.
[47] Jeng US, Su CH, Su CJ, Liao KF, Chuang WT, Lai YH, et al. J Appl Cryst 2010;43: 110–21.
[48] Müller-Buschbaum P, Gutmann JS, Wolkenhauer M, Kraus J, Stamm M, Smilgies D, et al. Macromolecules 2001;34:1369–75.
[49] Since the size of AFM tips may cause the shape of the tips to be convoluted with the surface features, the structural information (such as domain size and inter-domain distance) of nanodomains determined by AFM reveals a slight difference from that obtained by TEM and GISAXS.
[50] Stein GE, Kramer EJ, Li X, Wang J. Macromolecules 2007;40:2453–60.
[51] Stein GE, Cochran EW, Katsov K, Fredrickson GH, Kramer EJ, Li X, et al. Phys Rev Lett 2007;98:158302.
[52] Müller-Muschbaum P. Applications of synchrotron light to noncrystalline diffraction in materials and life sciences. In: Ezquerra TA, Garcia-Gutierrez MC, Nogales A, Gomez M, editors. A basic introduction to grazing incidence small angle X-ray scattering, vol. 776. Berlin: Spinger; 2009. p. 61–89 [Chapter 3].
[53] Liou JY, Sun YS. Macromolecules 2012;45:1963–71.
[54] Sun YS, Chien SW, Liou JY, Su CH, Liao KF. Polymer 2011;52:1180–90.
[55] Sun YS, Chien SW, Liou JY. Macromolecules 2010;43:7250–60.
[56] Zhu L, Huang P, Cheng SZD, Ge Q, Quirk RP, Thomas EL, et al. Phys Rev Lett 2001;86:6030–3.
[57] Zhu L, Huang P, Chen WY, Weng X, Cheng SZD, Ge Q, et al. Macromolecules 2003;36:3180–8.